

COSMOGLOBE DR1. III. First full-sky model of polarized synchrotron emission from all *WMAP* and *Planck* LFI data

D. Watts^{1*} and U. Fuskeland¹ et al.

Institute of Theoretical Astrophysics, University of Oslo, Blindern, Oslo, Norway

October 2, 2023

ABSTRACT

We present the first model of full-sky polarized synchrotron emission that is derived from all *WMAP* and *Planck* LFI frequency maps. The basis of this analysis are the end-to-end reprocessed COSMOGLOBE Data Release 1 sky maps presented in a companion paper, which have significantly lower instrumental systematics than the legacy products from each experiment. We find that the resulting polarized synchrotron amplitude map has an average noise rms of $2.4 \mu\text{K}$ at 22 GHz and a smoothing scale of 2° FWHM, which is 30 % lower than the recently released BEYONDPLANCK model that included only LFI+*WMAP* *Ka*–*V* data, and it is 45 % lower than the raw *WMAP* *K*-band. The mean *EE/BB* power spectrum ratio is 0.27 ± 0.02 , which agrees well with previous estimates from both *Planck* and QUIJOTE. Assuming a power law model for the synchrotron spectral energy density, we find a full-sky inverse noise-variance weighted mean of $\beta_s = -3.06 \pm 0.08$ between *WMAP* *K*-band and LFI 30 GHz, in good agreement with previous estimates. At high Galactic latitudes, however, we find $\beta_s = -3.31 \pm 0.08$, which is slightly steeper than most previous foregrounds-oriented estimates, but in good agreement with the *Planck* 2018 LFI CMB likelihood result of $\beta_s = -3.27 \pm 0.04$. For comparison, the corresponding full-sky and high-latitude estimates derived from the official *WMAP* and LFI products are $\beta_s = -3.44 \pm 0.08$ and $\beta_s = -3.71 \pm 0.08$, respectively. The latter values are clearly compromised by large-scale instrumental systematics in both *WMAP* and LFI. In summary, the novel COSMOGLOBE DR1 synchrotron model is both more sensitive and systematically cleaner than similar previous models, and it has a more complete error description that is defined by a set of Monte Carlo posterior samples. We believe that these products are preferable for all synchrotron-related scientific applications compared to the official maps, including simulation, forecasting and component separation.

Key words. ISM: general – Cosmology: observations, polarization, cosmic microwave background, diffuse radiation – Galaxy: general

Contents

1	Introduction
2	Data products
2.1	<i>WMAP</i> and <i>Planck</i> legacy products
2.2	COSMOGLOBE products
3	Polarized synchrotron amplitude
3.1	Comparison with independent datasets
3.2	Power spectra
4	Polarized synchrotron spectral indices
4.1	T-T plot analysis
4.1.1	Method
4.1.2	Results
4.2	Parametric component estimation
5	Discussion and conclusion
A	T-T Plots

1. Introduction

Understanding the polarization of the cosmic microwave background (CMB) is a primary focus of observational cosmology in

the coming decades. Following the success of the satellite-based *COBE*, *WMAP*, and *Planck* experiments, as well as sub-orbital experiments including, e.g., BICEP, ACT, SPT, Polarbear, and many others, the future LiteBIRD satellite and ground-based Simons Observatory (SO) and CMB-S4 experiments will create the most sensitive maps of the polarized sky yet, providing the most stringent constraints on primordial gravitational waves.

In the past decade, uncertainty on cosmological constraints has been limited not only by instrumental sensitivity, but by incomplete knowledge of the sky itself. Uncertainty in the sky model has been mitigated by designing experiments with broad frequency coverage, such as the *Wilkinson Microwave Anisotropy Probe* (*WMAP*) (Bennett et al. 2013) and *Planck* (Planck Collaboration I 2020), or analyzing maps from different experiments jointly, e.g., Bennett et al. (1996), Bennett et al. (2013), Planck Collaboration X (2016), and BICEP2/Keck Array and Planck Collaborations (2015), among many others. A major impediment to joint analyses is the difficulty of combining data with different survey strategies and incompletely characterized systematics. In order to maximize scientific throughput, one must either design an experiment that can characterize every relevant observable on its own, or jointly analyze different datasets in the same joint framework.

The BEYONDPLANCK project achieved this joint analysis by combining external data, specifically, the Haslam 408 MHz map (Haslam et al. 1982), *WMAP* *Ka*–*V* bands, *Planck* 353 GHz in polarization, and *Planck* 857 GHz in intensity, while analyzing

* Corresponding author: D. Watts; duncanwa@astro.uio.no

the *Planck* 30, 44, and 70 GHz time-ordered data (TOD) (BeyondPlanck Collaboration 2023). The *Planck* LFI experiment showed that raw detector sensitivity was not enough to obtain high-fidelity sky maps; Planck Collaboration II (2020) found that the detector gain solution depended on the assumed polarization and intensity of the sky. To break this circular dependency, the BEYONDPLANCK framework solved for the intrinsic sky signal and instrumental parameters iteratively, providing an accurate model of the entire system with full error propagation. By leveraging external data, BEYONDPLANCK was able to create *Planck* LFI maps of cosmological quality, while generating a robust model of the foreground sky.

The COSMOGLOBE project¹ expanded the BEYONDPLANCK analysis by processing *WMAP* K–W-band TOD jointly with *Planck* LFI TOD. This framework, fully described in Watts et al. (2023b) and Watts et al. (2023a), not only improved the quality of the *WMAP* maps themselves, but provided the most robust full-sky model of low frequency polarized emission available to date. In particular, poorly-measured modes due to transmission imbalance (Jarosik et al. 2007) have been effectively marginalized over, in large part due to the use of a global sky model which was not used in the fiducial *WMAP* analyses. The removal of poorly measured modes alone will improve Galactic modelling for years to come, as the current state-of-the-art models use *WMAP* K-band (23 GHz) maps as polarized synchrotron templates for modeling of synchrotron without any mitigation of the poorly-measured modes (Delabrouille et al. 2013; Thorne et al. 2017; Zonca et al. 2021).

In order to make use of the synchrotron model, we require robust estimates of the spectral behavior. Fundamental behaviors, such as the spectral index as a function of frequency, spatial decorrelation, and even the functional form of the SED, are yet to be fully characterized observationally. Modern attempts have been stymied by the lack of high signal-to-noise data; de Belsunce et al. (2022), for example, find spectral indices ranging from -5 to -1 , discrepant with predictions from direct measurements of the cosmic ray energy spectrum of 2 – 3 (Rybicki & Lightman 1985; Orlando & Strong 2013; Neronov et al. 2017). This discrepancy is largely due to inadequate data coverage, requiring higher signal-to-noise datasets that have not yet been generated. Therefore, any conclusions about the distribution of the polarized synchrotron spectral index must be verified through multiple independent analysis methods and data choices.

While the combination of as many datasets as possible would help to constrain polarized synchrotron’s large-scale properties, long-standing discrepancies complicates this. As shown in, e.g., Planck Collaboration X (2016) and Weiland et al. (2018), there are discrepancies in the polarization measurements of *WMAP* and *Planck*, partially due to unconvolved gain solutions (Planck Collaboration II 2020) and poorly measured mapmaking modes (Bennett et al. 2013). BeyondPlanck Collaboration (2023) resolved the unconvolved gain solution creating low-systematics LFI maps for the first time, while Watts et al. (2023b) demonstrated that the poorly measured modes in *WMAP* could be removed through joint processing, while identifying a similar systematic effect that could mimic the previously-reported effect. While Watts et al. (2023a) has demonstrated that the polarized maps from these two experiments are now consistent at the white noise level, the new maps must be validated first. As noted in, for example, Weiland et al. (2022), simply using a different analysis pipelines can result in different estimations of the underlying frequency map. As such, we take care to appropriately marginalize

over instrumental effects in our spectral analysis, and attempt to find the physical mechanism for the differences between different pipelines.

This work is organized as follows. In Section 2, we provide a brief overview of the data products and the COSMOGLOBE data processing. Section 3 discusses the polarized amplitude of the COSMOGLOBE synchrotron model, its overall uncertainty, the power spectrum properties compared to external products. Section 4 estimates the synchrotron spectral index using both the model-independent T-T plot method and Gibbs sampling using Commander, followed by discussions and conclusions in Sect. 5.

2. Data products

In this paper, we investigate the spatial variation of the polarized synchrotron spectral index, with an emphasis on the comparison between legacy maps against the COSMOGLOBE results. The data products used are the *WMAP* and *Planck* LFI maps, with most of the statistical weight coming from 23–33 GHz. These frequencies are low enough that we can treat them as synchrotron tracers and hence ignore thermal dust and the CMB, but not so low as we need to take into account effects like Faraday rotation (Fuskeland et al. 2021). The legacy data products and the data products from the COSMOGLOBE *WMAP* reanalysis (Watts et al. 2023a), are described in the two following sections.

2.1. WMAP and Planck legacy products

WMAP was a NASA-funded satellite mission that observed from August 2001 to August 2010, designed to characterize the microwave sky well enough to measure the primary CMB anisotropies across the full sky down to a resolution of $13'$. Using a differential scanning strategy inspired by COBE/DMR, *WMAP* produced maps of the sky at 23 (*K*), 33 (*Ka*), 41 (*Q*), 61 (*V*), and 94 GHz (*W*) in both polarization and intensity (Bennett et al. 2013), with angular resolutions of $53'$ at 23 GHz to $13'$ at 94 GHz. The maps are available on the LAMBDA website.²

The *Planck* Low Frequency Instrument (LFI) produced 30, 44, and 70 GHz maps in both intensity and polarization, while the High Frequency Instrument (HFI) produced 100, 143, 217, 353 GHz maps in polarization and intensity, and 545 and 857 GHz maps in intensity alone. The LFI data in particular are similar to the *WMAP* data, with higher angular resolutions of $30'$, $20'$, and $13'$ for 30, 44, and 70 GHz, and with higher sensitivity. Although the detector design was similar, LFI observed with a single horn, and observed in rings closely aligned with the ecliptic longitude. The legacy datasets, PR3 (Planck Collaboration I 2020) and PR4 (Planck Collaboration Int. LVII 2020), are both publicly available on the *Planck* Legacy Archive (PLA).³

2.2. COSMOGLOBE products

The goal of COSMOGLOBE is to perform joint end-to-end analyses on several data sets jointly, preferably beginning from raw TOD. Doing this can help to break the degeneracies of the different data sets, and in general reduced the amplitude of systematic effects. The analysis in BeyondPlanck Collaboration (2023) and Watts et al. (2023a) was performed on raw TOD, producing cosmological parameters using the Bayesian Gibbs sampler,

² https://lambda.gsfc.nasa.gov/product/wmap/dr5/m_products.html

³ <https://pla.esac.esa.int/>



Fig. 1. Polarized intensity of (top): *WMAP* *K*-band, (middle): *Planck* 30 GHz, and (bottom): synchrotron amplitude from COSMOGLOBE Gibbs chain, all evaluated at 30 GHz with a resolution of 72'. The leftmost column is a 10° width square centered at one of the lowest signal-to-noise regions in each of the maps, while the rightmost column shows the rms noise for the frequency maps and the posterior standard deviation of the synchrotron amplitude.

Commander3 (Galloway et al. 2023). The data products produced in these analysis account for the complex interactions between the instrument, the microwave sky, and its constituent components self-consistently. The full products from this analysis and individual maps are available on the COSMOGLOBE website.⁴

This paper makes use of COSMOGLOBE end products produced by the reanalysis of the *WMAP* and *Planck* LFI TODs (Watts et al. 2023a). That paper produced improved *WMAP* and *Planck* LFI maps, which we will use compare our results to those produced by legacy data. Although most of the results in Watts et al. (2023a) use the posterior mean of the Gibbs chain, here we make use of the entire sample of 500 sets of frequency maps. This allows us to fully marginalize over the low-level systematic parameters, quantifying the amount instrumental processing affects the

CMB, synchrotron, thermal dust, free-free emission, anomalous microwave emission, and radio point sources, the first three of which we model as polarized in our sky model.

When using external data for polarized foreground cleaning, the choices for high signal-to-noise full sky constraints are either *WMAP* *K*-band, *Planck* LFI 30 GHz, or models derived from combinations of these data, as in, e.g., COSMOGLOBE. From the perspective of pure statistical uncertainty, a combination of multiple independent datasets would yield component maps that are more sensitive than each individual component. However, unmodeled systematic uncertainties in the underlying datasets, left untreated, can induce map effects that can leak into astrophysics and cosmological constraints. As shown in Watts et al. (2023a), a single sky model that all datasets are calibrated against improves the low-level instrumental processing, and allowing for degeneracies, such as poorly-measured modes in *WMAP* and differential gain uncertainty in LFI, to be broken. Within the COSMOGLOBE DR1 framework, the polarization maps from *WMAP* and *Planck* LFI are consistent with each other at the 10 μK level, consistent with the instrumental white noise of the datasets.

The COSMOGLOBE DR1 frequency maps are free from previously reported systematics, and are consistent between different frequencies and instruments. Therefore, a coherent model of polarized synchrotron emission can be made by combining these two different datasets. The polarized spectral amplitude determined from COSMOGLOBE fully utilizes the *Planck* and *WMAP*

⁴ <https://www.cosmoglobe.uio.no/products/cosmoglobe-dr1.html>

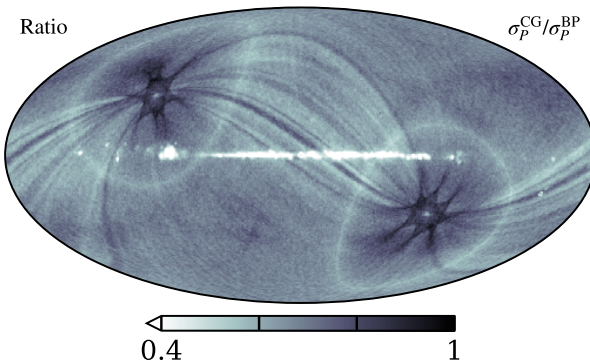


Fig. 2. COSMOGLOBE posterior standard deviation divided by BEYONDPLANCK posterior standard deviation.

joint reprocessed data, as shown in Fig. 1. We plot the total polarized amplitude $P = \sqrt{Q^2 + U^2}$ for ease of comparison. The visible noise bias from plotting this positive definite quantity highlights the reduction in the noise level in the COSMOGLOBE synchrotron map as compared to the *K*-band and 30 GHz maps.

The *WMAP* *K*-band data and LFI 30 GHz data, as the highest signal-to-noise full-sky polarized maps of Galactic synchrotron emission, are the main contributors to our knowledge of the polarized amplitude. The slightly higher angular resolution 30 GHz map has lower sensitivity than the *K*-band data, but by combining the multi-resolution maps we are able to produce a clean map of the synchrotron emission evaluated at 30 GHz with a FWHM of 1° .

The synchrotron amplitude maps from end-to-end processing, BEYONDPLANCK and COSMOGLOBE, contain slightly different datasets, but sample the instrumental properties and sky properties jointly. Of these maps, BEYONDPLANCK has lower resolution and higher noise, in large part because COSMOGLOBE is able to use the reprocessed *WMAP* *K*-band map. The COSMOGLOBE synchrotron map has a mean posterior rms of $2.4\,\mu\text{K}$, a marked improvement over the BEYONDPLANCK map, as shown in Fig. 2. The rms map itself contains high signal-to-noise regions corresponding to the *WMAP* circles about the ecliptic poles as well as the *Planck* rings and multiple ecliptic polar crossings. The main clear astrophysical variation comes in the forms of a thin region about the Galactic plane and several low-latitude point sources. Much of the improvement can be seen more clearly when taking the ratio of the posterior rms's, as in Fig. 2. As expected, the regions with the lowest ratios correspond to the deep *WMAP* observations and the Galactic plane, which benefit from the high signal-to-noise of the *K*-band data. Regions with nearly identical rms include regions with the highest *Planck* depth, such as the ecliptic poles, and regions less deeply observed by *WMAP*, corresponding to planet crossings and artifacts from the processing mask. Notably, stripes corresponding to the *Planck* scan strategy also show improvement respect to BEYONDPLANCK. This is due to the interaction between the sky model and LFI's instrumental parameters – with the high signal-to-noise *K*-band data, the sky model becomes more stable, and LFI's relative gain solution becomes better determined.

To quantify the noise improvement in the synchrotron maps over pure templates based on either *K*-band or 30 GHz maps, we compare the posterior standard deviation of the COSMOGLOBE synchrotron map with the frequency maps' rms values. The posterior standard deviation maps are $\lesssim 1\,\mu\text{K}$ for *K*-band, while

temperature-to-polarization uncertainty in 30 GHz contributes at the $2\,\mu\text{K}$ level (see, e.g., Watts et al. 2023a and Basyrov et al. 2023 for further details). An informative prior of $D_\ell = 200 e^{-\ell(\ell+1)\sigma^2(30')}$ μK^2 is applied during polarized synchrotron amplitude fitting, essentially downweighting low signal-to-noise fluctuations at angular scales $\lesssim 30'$, or $\ell \gtrsim 360$ (Svalheim et al. 2023a). Therefore, the rms noise contributions are relevant at roughly $N_{\text{side}} = 128$. We additionally simulate white noise smoothed to $72'$ and scaled to 30 GHz assuming $\beta_s = -3.1$, consistent with the post-processed synchrotron map, which we display in the right column of Fig. 1.

At these resolutions, the mean rms for *K*-band and 30 GHz are $4.8\,\mu\text{K}$ and $4.7\,\mu\text{K}$ respectively, compared to the mean value of $3.4\,\mu\text{K}$ for the COSMOGLOBE DR1 synchrotron map, consistent with adding the scaled maps in quadrature. While this may seem obvious on its face, the combination of *WMAP* *K*-band and *Planck* 30 GHz is not straightforward due to instrumental effects that remain in the maps, notably poorly measured modes in *WMAP* (Bennett et al. 2013; Weiland et al. 2018) and gain uncertainty in *Planck* (Planck Collaboration II 2020). These effects remain in the official *WMAP9* (Bennett et al. 2013) and *Planck* PR3/PR4 (Planck Collaboration II 2020; Planck Collaboration Int. LVII 2020) maps, making combination of these datasets unsuitable for Galactic science and cosmological analyses. However, the end-to-end BEYONDPLANCK (BeyondPlanck Collaboration 2023) products effectively removed the gain uncertainty modes from the *Planck* LFI maps, and the COSMOGLOBE DR1 results (Watts et al. 2023a) are free from the poorly measured modes. As shown in Fig. 46 of Watts et al. (2023a), the *Planck* 30 GHz and the *WMAP* *K*-band are consistent with each other at the $10\,\mu\text{K}$ level, indicating that the maps are consistent with each other down to the white noise level.

This polarized synchrotron map, derived from consistent datasets, has a white noise level 29 % lower than both the *K*-band map and the 30 GHz map, with minimal systematic uncertainties in the posterior standard deviation. Therefore, the synchrotron map derived from the COSMOGLOBE DR1 Gibbs chain should be used for the characterization and removal of polarized synchrotron emission between 23–90 GHz. While the COSMOGLOBE pipeline produces samples of polarized synchrotron emission, the spatial variation of the spectral index is poorly determined within the Gibbs chain. To mitigate the poor Monte Carlo Markov Chain (MCMC) convergence of the spectral indices, the COSMOGLOBE DR1 sampled the spectral index from a prior distribution, $\beta_s \sim \mathcal{N}(-3.15, 0.05)$. Improvements within the Commander3 framework will require more high signal-to-noise data and algorithmic improvements within the codebase.

3.1. Comparison with independent datasets

As a check on the polarized synchrotron amplitude, we compare the COSMOGLOBE polarized synchrotron map with the frequency maps produced in the main DR1 chain, paying special attention to maps with the highest polarized synchrotron signal-to-noise ratio, *WMAP* *K*- and *Ka*-band, and LFI 30 and 44 GHz. These maps should agree by virtue of being produced in the same analysis framework. We compare with the *WMAP9*, PR3, and PR4 maps. Of these, the *WMAP9* results can be considered the most independent, as the results were produced with no sky model assumptions, and were produced before the *Planck* polarized maps were publically available, thus making the analysis completely unbiased. The PR3 and PR4 maps should also be independent of the *WMAP9* results, while the PR4 results share information

by virtue of the joint processing framework in which the *Planck* LFI and HFI data were produced.

Using the polarized synchrotron model generated in the main COSMOGLOBE DR1 chain, we can evaluate the synchrotron emission at each frequency and compare it with the maps produced by various different processing pipelines. We evaluate the COSMOGLOBE sky model using the `cosmoglobe` Python package to evaluate the sky model using the full bandpass information of each instrument.⁵ Visual inspection of the data with the synchrotron model subtracted and smoothed to a common 5° Gaussian beam provides a robust check on the quality of the model and the underlying data.

As shown in Watts et al. (2023a) and the first and third rows of Fig. 3, the synchrotron model matches the sky model within 5 μK across the sky, with no signature of observational artifacts in the maps. In contrast, the *WMAP*, PR3, and PR4 residuals show known observational residuals in each of the maps. In particular, the *WMAP* maps show artifacts of the poorly-measured modes due to transmission imbalance in the differential horns (Jarosik et al. 2007; Bennett et al. 2013), while the PR3 and PR4 differences mostly due to relative gain errors (Planck Collaboration II 2020; Planck Collaboration Int. LVII 2020).

The *WMAP9* *K*-band residuals, and to a lesser extent the *WMAP9* *Ka*-band residuals, are largely dominated by the imbalance modes, and virtually no trace of them can be found in the COSMOGLOBE residuals. Most of the residuals are associated with the Galactic plane and diffuse structure uncorrelated with the *WMAP* observation strategy. The positive excess in the *Ka* Stokes *Q* map could be due to as yet unmitigated data processing artifacts. While a similar large-scale excess can also be seen in the LFI 30 and 44 GHz Stokes *Q* maps, the signature strongly resembles the bandpass correction in *WMAP K*-band, suggesting incomplete treatment of bandpasses could be contributing to this large-scale signal. The LFI residuals, while much improved, still show traces residuals, especially near the Galactic center, that are somewhat correlated with the gain correction templates, but not at a level that high Galactic latitude features can be identified.

As the scale of instrumental residuals have been reduced to below the white noise level for each of the synchrotron-dominated full-sky polarization maps, we are now able to associate the residuals with potential modifications to the sky model. Specifically, the COSMOGLOBE DR1 processing sampled a spatially constant β_s with a final mean of $\beta_s = -3.15$. In Sec. 4, we will determine the extent to which true on-sky variation can be determined based on these maps.

3.2. Power spectra

Due to the importance of foreground removal for precise primordial gravitational wave measurement, the ratio of synchrotron B-modes to E-modes has long been studied, and has been consistently noted to be less than one (Page et al. 2007; Planck Collaboration X 2016; Planck Collaboration IV 2018). The physical mechanism for this has been discussed in the context of Galactic magnetic fields and polarized thermal dust, but similar mechanisms are likely to be in play for synchrotron polarization.

To estimate the power spectra without a noise bias, we performed a Commander3 run using half-mission splits with odd-numbered scans and even-numbered scans being analyzed in runs labeled HM1 and HM2, analogous to the *Planck* “half-mission” splits. Each of these chains were performed using the

Table 1. Best-fit power law parameters to the synchrotron estimates evaluated at 30 GHz, using half-mission splits with NaMaster.

	PR3	COSMOGLOBE
$A_s^{EE} [\mu\text{K}^2]$. . .	2.39 ± 0.07	2.35 ± 0.05
$A_s^{BB} [\mu\text{K}^2]$. . .	1.09 ± 0.06	0.94 ± 0.04
A_s^{BB}/A_s^{EE}	0.46 ± 0.03	0.40 ± 0.02
α_s^{EE}	-0.81 ± 0.02	-0.87 ± 0.02
α_s^{BB}	-0.80 ± 0.03	-0.81 ± 0.03

same data as in the main COSMOGLOBE chain, with 200 samples each.⁶ The highest quality similar half-mission splits that are publicly available are from the *Planck* PR3 analysis, as discussed in Planck Collaboration IV (2018). We therefore compute power spectra from the PR3 results and compare them directly with the COSMOGLOBE HM splits. We needed to run a special Commander3 chain, splitting the TODs into half mission, with all odd-numbered scans being processed in chain HM1, and all even-numbered scans in HM2, and produced 200 samples each.

We perform the power spectrum using NaMaster (Alonso et al. 2019) using the *Planck* 2018 common polarization mask with $f_{\text{sky}} = 0.78$ and using 1° apodization. To quantify the uncertainty, we take the cross spectrum for each pair of Gibbs samples from the adjacent chain, and report the 68 % confidence intervals on this posterior. The power spectra are displayed in Fig. 4, and the standard deviation is computed using the within-bin variance of each bin, with the posterior standard deviation of the Gibbs chain added in quadrature for the COSMOGLOBE spectra. Other than the very lowest and very highest multipole bins, there is good per-multipole agreement between both the PR3 and COSMOGLOBE DR1 spectra.

Following Planck Collaboration IV (2018), we perform power law fits to the power spectra of the form $\mathcal{D}_{\ell}^{\text{EE}/\text{BB}} = A_s^{\text{EE}/\text{BB}}(\ell/80)^{\alpha}$, using multipoles $\ell \in [2, 140]$. The 68 % confidence intervals for each quantity, including the $A_s^{\text{BB}}/A_s^{\text{EE}}$ ratio, are reported in Table 1. The primary differences between the fits to the two datasets are $\sim 2 \sigma$ discrepancies in the A_s^{BB} and α_s^{EE} fits, while all others are consistent within $\simeq 0.5 \sigma$. The primary drivers of these differences are lower $\mathcal{D}_{\ell}^{\text{BB}}$ and higher $\mathcal{D}_{\ell}^{\text{EE}}$ in the lowest bins. These fit parameters yield a $\lesssim 2 \sigma$ lower $A_s^{\text{BB}}/A_s^{\text{EE}}$ value of 0.40. While this is higher than the published value of 0.34 using the same binning and mask of Planck Collaboration IV (2018), we obtained a higher value of 0.46 using very similar processing. Despite the discrepancies between the processing in this paper and Planck Collaboration IV (2018), it is clear that the COSMOGLOBE DR1 ratio is lower than that of *Planck* PR3 when processed in our framework.

4. Polarized synchrotron spectral indices

The determination of polarized synchrotron spectral index variation across the sky has been studied in detail over the past decade using several different data combinations. Although the small-scale details vary, nearly every analysis has $\beta_s \simeq 2.8$ in the Galactic plane and $\beta_s \sim -3.3$ in high Galactic latitudes (Fuskeland et al. 2014; Krachmalnicoff et al. 2018; Fuskeland et al. 2021; Weiland et al. 2022), with the exception of QUIJOTE (Rubiño-Martín et al. 2023; de la Hoz et al. 2023), who find a slightly flatter spectral index along the Galactic plane. However, true spatial variations beyond the high-latitude and low-latitude

⁵ <https://cosmoglobe.readthedocs.io/en/latest/tutorials/skymodel.html>

⁶ These products can be found at cosmoglobe.uio.no.



Fig. 3. Residuals with respect to the COSMOGLOBE DR1 sky model evaluated at 5° , with common colorscale of $\pm 5 \mu\text{K}$. COSMOGLOBE maps are labeled CG, *Planck* 2018 maps are labeled PR3, and the legacy *WMAP*9 maps are labeled WMAP.

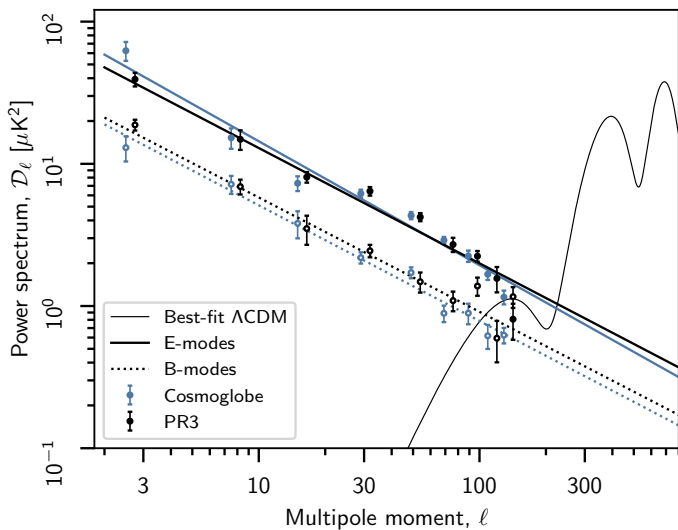


Fig. 4. Half-mission splits of synchrotron for *Planck* PR3 (black) and COSMOGLOBE DR1 (black). Filled circles correspond to E-modes, while empty circles correspond to B-modes.

regions have been difficult to determine. Both Fuskeland et al. (2014) and Weiland et al. (2022) report oscillations with Galactic longitude close to the Galactic plane, but high-latitude regions variations are more difficult to determine, and tend to depend on the specific dataset chosen and the analysis method chosen.

A fundamental challenge in spectral index estimation is due to the fact that every difference between two channels can be as-

sociated with a spectral index variation if not accounted for fully. Therefore, it is necessary to not only make sure that results are robust towards data selection, but also to ensure that differences between results are not due to instrumental effects.

In order to test for and mitigate these effects, we perform two approaches, a T-T plot analysis in Sect. 4.1 and a Gibbs sampling analysis using `Commander1` in Sect. 4.2. Sect. 4.1 focuses on pairs of channels to better isolate potential unmodeled systematic effects, while Sect. 4.2 uses all *WMAP* and LFI channels plus *Planck* 353 GHz to maximize the joint statistical weight of all available data.

4.1. T-T plot analysis

As pointed out in Wehus et al. (2013), unmodeled instrumental effects, including polarization angle mismatch between detectors and elliptical beams, can induce a polarization angle-dependent spectral index that is especially prominent in point sources. These effects can often be identified by performing analysis as a function of polarization angle. As both *WMAP* and *Planck* have asymmetric beam responses, this effect has long been noticed in the data, contaminating spectral index estimates. Performing a “temperature-temperature” (T-T) analysis as a function of polarization angle, shows the magnitude of this effect in the COSMOGLOBE, *WMAP9*, and *Planck* PR4 data.

4.1.1. Method

Following Fuskeland et al. (2014) and Fuskeland et al. (2021), we apply linear regression via the T-T plot method, in which



Fig. 5. Spectral index regions as defined in Fuskeland et al. (2014). The most prominent point sources are masked out and shown in grey circular areas.

spectral indices can be estimated over extended regions with approximately constant spectral indices. In this approach, our data model for two frequencies is

$$\mathbf{m}_\nu = \mathbf{m}_{\nu_0} \left(\frac{\nu}{\nu_0} \right)^\beta + o_\nu + \mathbf{n}_\nu, \quad (1)$$

where \mathbf{m}_ν is a spatially varying amplitude map, ν_0 is the reference frequency, β the power law between the two frequencies, o_ν the spatially constant offset per band, and \mathbf{n}_ν the noise. In the case of noiseless data with no offset, the spectral index may be estimated using a simple ratio,

$$\frac{m_{\nu_1,p}}{m_{\nu_2,p}} = \left(\frac{\nu_1}{\nu_2} \right)^{\beta_{s,p}} \Rightarrow \beta_{s,p} = \frac{\ln(m_{\nu_1,p}/m_{\nu_2,p})}{\ln(\nu_1/\nu_2)}. \quad (2)$$

The standard T-T plot method performs a linear regression $\mathbf{m}_{\nu_1} = a\mathbf{m}_{\nu_2} + b$, and associates β_s with $\ln a / \ln(\nu_1/\nu_2)$. More care must be taken when the noise amplitudes in both maps are comparable, so we adopt the effective variance method of Orear (1982) as implemented by Fuskeland et al. (2014).

For the T-T plot analysis, we focus exclusively on bands between 23 and 33 GHz. As in Fuskeland et al. (2014), we use the WMAP K and Ka band Stokes Q and U parameter maps at 23 GHz and 33 GHz. The respective effective frequencies used are 22.45 GHz and 32.64 GHz. The maps originally at a HEALPix pixelization of $N_{\text{side}} = 512$ are downgraded to $N_{\text{side}} = 64$ and smoothed to a common resolution of 1° FWHM. The *Planck* data products used are the 30 GHz Stokes Q and U maps, with an effective frequency of 28.4 GHz. Both the BEYONDPLANCK and COSMOGLOBE products are natively at $N_{\text{side}} = 512$, while for the *Planck* PR4, it is 1024, while for the WMAP products, we downgraded the maps to $N_{\text{side}} = 64$ and smoothed to 1° FWHM.

The uncertainty of the spectral indices is calculated as the minimum of the uncertainties in each rotation angle, and region. As in Fuskeland et al. (2021), a systematic uncertainty that takes into account the variation of β over rotation angle; $[\max(\beta_\alpha) - \min(\beta_\alpha)]/2$ is added in quadrature to the statistical uncertainty. For the COSMOGLOBE analyses we have a whole suite of maps represented by the individual samples instead of just one mean map. Here the standard deviation of the spectral indices of the samples is also added in quadrature to represent an additional systematic uncertainty. This enables us to have a better propagation of uncertainties from the maps to the final spectral indices.

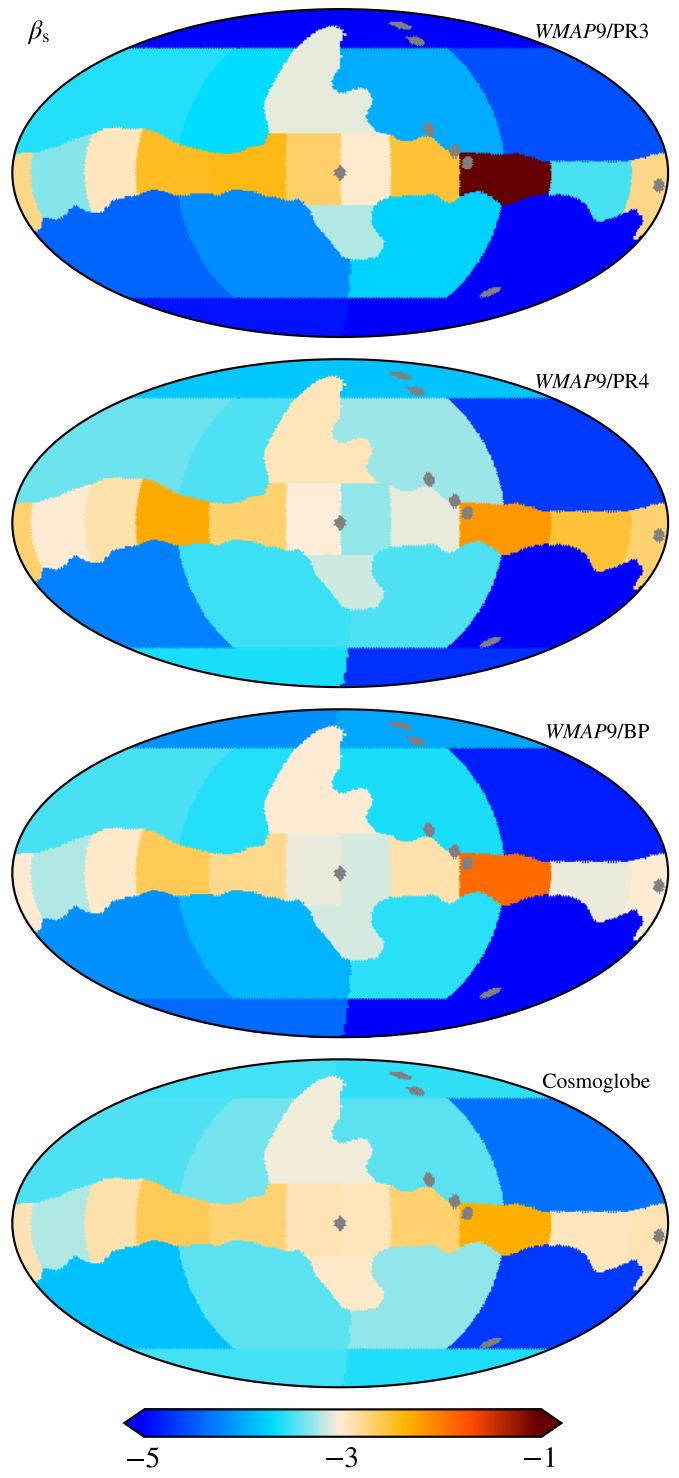


Fig. 6. Spatial variation of the synchrotron spectral index, computed using T-T plot between the (from top to bottom) WMAP9 23 GHz and *Planck* 2018 30 GHz, WMAP9 23 GHz and *Planck* DR4 30 GHz, WMAP9 23 GHz and BEYONDPLANCK 30 GHz, and COSMOGLOBE 23 GHz and COSMOGLOBE 30 GHz. The spectral index is inverse variance weighted over rotation angle, and in the COSMOGLOBE case also samples.

4.1.2. Results

We start by looking at the results from the T-T plot method applied to the K -band (23 GHz) and 30 GHz maps. We apply the method to the 24 regions to see the spatial variation of the po-

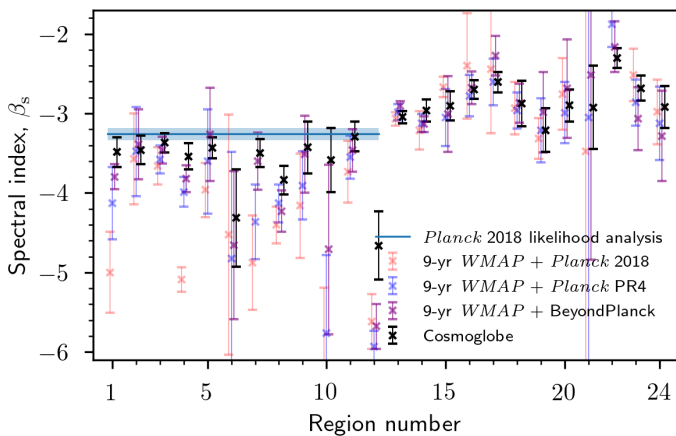


Fig. 7. The synchrotron spectral index as a function of region number, computed using T-T plot between the 9-yr *WMAP* 23 GHz and *Planck* 2018 30 GHz (red), 9-yr *WMAP* 23 GHz and *Planck* DR4 30 GHz (blue), 9-yr *WMAP* 23 GHz and BEYONDPLANCK 30 GHz (purple), and COSMOGLOBE 23 GHz and COSMOGLOBE 30 GHz (black). The spectral index is inverse variance weighted over rotation angles, and samples. The horizontal line in the high latitude regions corresponds to the estimated spectral index values from the *Planck* 2018 likelihood analysis ([Planck Collaboration V 2020](#)).

larized synchrotron spectral index. The three top maps in Fig. 6 shows the T-T plot method using *WMAP9* *K*-band and three incarnations of the *Planck* 30 GHz maps; PR3, PR4, and BEYONDPLANCK. The bottom map shows the results using the improved maps from the COSMOGLOBE analysis; COSMOGLOBE *K*-band and 30 GHz. The spectral indices are inverse variance weighted over rotation angle, and in the COSMOGLOBE case also samples. Some of the most bright point sources have been masked out using grey. We see an overall improvement in the results of the spectral index, from regions with extreme values in the top map represented by dark red and blue values, with colors gradually fading in the lower figures. The range in the plot is quite wide for spectral indices, and goes from -5 to -1 . This improvement in the value of the spectral index, and therefore also the underlying data, is especially prominent in the high Galactic regions, as well as region number 22 along the Galactic plane.

The same results are also shown in Fig. 7, with the spectral indices plotted as a function of region number. The different datasets are shown in different colors, and with the same order as the four maps in Fig. 6. Here we have also included one sigma uncertainties as errorbars as described in Sect. 4.1.1. We also plot the estimated spectral index range for high Galactic regions, in our case represented by regions 1–12, as forecasted by the likelihood analysis in Figure 22 of [Planck Collaboration V \(2020\)](#). We see with each iteration of the data processing, the region estimates draw closer to this line. For a more detailed study of each of the regions, we refer the reader to the Appendix, where we have shown the corresponding T-T scatterplots (Fig. A.1) and the spectral index as a function of rotation angle (Fig. A.2) for all 24 regions.

As a second part of this T-T plot analysis we apply the method on *K*-band and *Ka*-band maps. For the *WMAP* data, this analysis was already performed in [Fuskeland et al. \(2014\)](#), so here we only present results using the new COSMOGLOBE data. First, as a consistency check, in Fig. 8 we plot the spectral indices for all 24 regions in the form of COSMOGLOBE *K*/30 GHz versus COSMOGLOBE *K*/*Ka*. We see that for the regions in the north and south Galactic spurs, and along the Galactic plane (regions

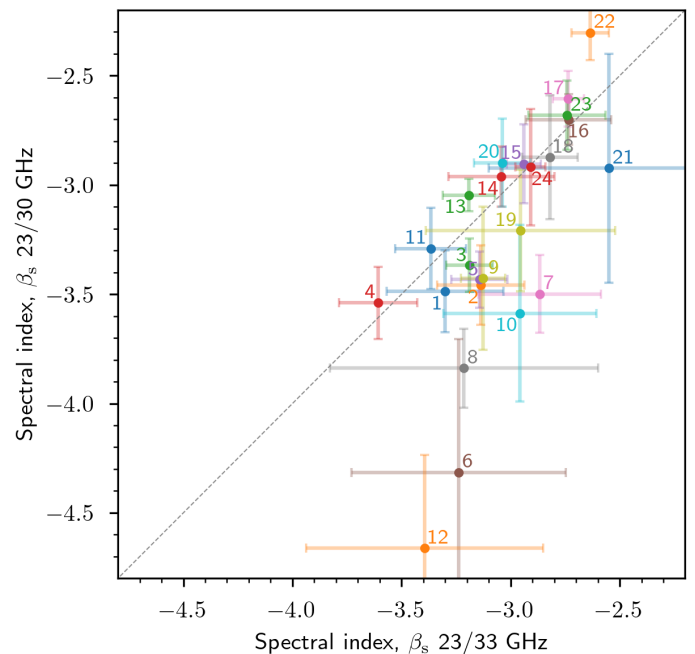


Fig. 8. Synchrotron spectral index computed using T-T plot with the COSMOGLOBE 23 GHz and 30 GHz data versus COSMOGLOBE 23 GHz and 33 GHz data for the 24 regions.

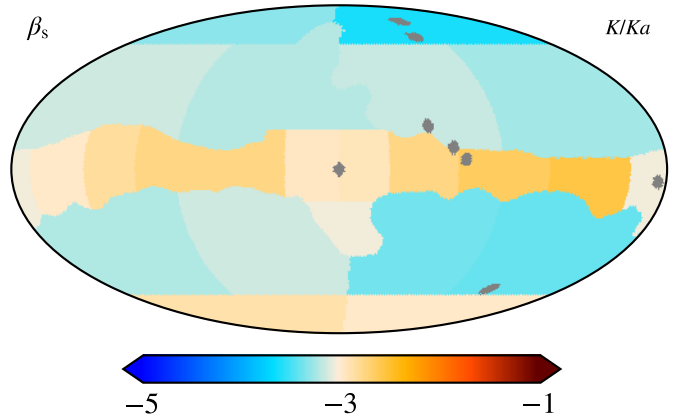


Fig. 9. Spatial variation of the synchrotron spectral index, computed using T-T plot between the COSMOGLOBE *WMAP* *K*- and *Ka*-band. The spectral index is inverse variance weighted over rotation angle and samples.

13–24), there is a good agreement between the spectral indices obtained by the two pairs of datasets. Regions 1–12, all of which are high-latitude regions with low signal-to-noise, are all consistent with the two data combinations, with the most prominent outliers, regions 6 and 12, the regions with the lowest signal-to-noise ratio.

In Fig. 9 the value of the spectral indices is shown for the 24 regions. We see here that the colors are even fainter than the COSMOGLOBE *K*-band versus 30 GHz values (the bottom figure in Fig. 6), meaning there are fewer outliers with respect to a standard value in the range around -3 . This is especially visible in the regions with lowest signal to noise, like regions 6, 8 and 12, at high latitude.

4.2. Parametric component estimation

Here we use Commander1⁷ to perform pixel-based component separation on maps smoothed to a common resolution of 5° and at $N_{\text{side}} = 64$. For this analysis, we perform 100 pixel-based Commander1 Gibbs samples on each of the 500 COSMOGLOBE DR1 Gibbs samples produced by Commander3. This allows us to decompose the pure statistical error assuming white noise alone for each of the 100 Commander1 samples, while changes between each main DR1 sample show the effects of low-level instrumental processing, commonly called “systematic” uncertainty. In these analyses, we use the same polarized bands as in the main CG DR1 analysis, namely *WMAP*, *Planck* LFI, and *Planck* 353 GHz. We use a prior $\beta_s \sim \mathcal{N}(-3.1, 0.1)$ for the synchrotron spectral index, while for dust we use a constant spectral index of $\beta_d = 1.55$ and the dust map T_d from [Planck Collaboration X \(2016\)](#).

We used the same data model as in COSMOGLOBE DR1, but allow for spatially varying β_s in two different forms. First, we performed a fit with β_s varying according to the pixels as in the T-T analysis. We find that for such large regions, there is very little effect due to the prior, and in particular find a maximum shift of 0.3 between a prior of $\mathcal{N}(-3.5, 0.1)$ and $\mathcal{N}(-2.7, 0.1)$. We add this difference in quadrature to the uncertainty due to... We also compare the reported β_s maps from QUIJOTE ([de la Hoz et al. 2023](#)) and CLASS ([Eimer et al. 2023](#)). We choose these maps because they are to this date the best publicly available available synchrotron spectral index maps available that are not affected by Faraday rotation off the Galactic plane, as in S-PASS ([Krachmalnicoff et al. 2018; Fuskeland et al. 2021](#)). The delivered β_s maps are pixelized at $N_{\text{side}} = 64$ and 32, respectively, with associated uncertainty maps taking into account the expected instrumental noise levels. We take an inverse-weighted average of the respective maps and report the weighted standard error within each region, displayed in Fig. 10.

In general, the uncertainties in our analysis are smaller than each of the other published results, each for slightly different reasons. First, the T-T analyses will inherently have less constraining power than a full likelihood analysis, as this approach only uses two frequency channels via a linear regression, so the uncertainty is determined by the noise level in each frequency channel and the inherent variation within a given sky region. Beyond that, the T-T plot in this paper marginalizes over dependence on the polarization angle α , and by design accentuates systematic effects, predominantly beam ellipticity. Finally, the QUIJOTE analysis is most similar in data choice (MFI 11/13 GHz, *WMAP9 K/Ka*, *Planck PR4*) and methodology (B-SeCRET; [de la Hoz et al. 2022](#)), but still yields higher uncertainty than the Commander1 spectral index region analysis. This is most likely due to different spatial resolution and modeling choices; the Commander1 analysis presented here is performed at 5° resolution versus the 2° resolution per-pixel analysis in [de la Hoz et al. \(2023\)](#). In addition, [de la Hoz et al. \(2023\)](#) sampled for β_d and T_d with priors $\mathcal{N}(1.55, 0.1)$ and $\mathcal{N}(21, 3)$ while using a relatively wide prior on β_s of $\mathcal{N}(-3.1, 0.3)$.

At high Galactic latitudes (regions 1–12), there is good agreement between each of the treatments, and all values are consistent with a single constant value. In the north and south polar spur (regions 13 and 14) there is excellent agreement between all of the pipelines, while along the Galactic plane (regions 15–24), there are mild discrepancies between the methodologies, in particular a less distinct amount of periodic structure as a function of Galactic latitude.

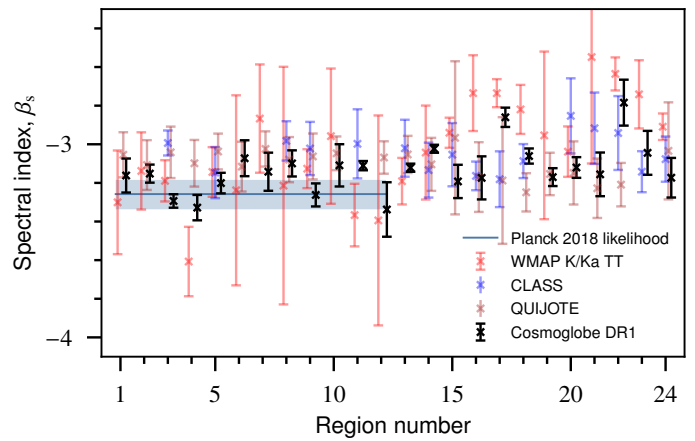


Fig. 10. Spectral index from the Commander1, T-T plots with *K/Ka*, the QUIJOTE estimates, and the CLASS estimates

To more finely probe the spatial variation of β_s , we perform a second Commander1 analysis with identical data and model choices, except the β_s are allowed to vary with a prior of $\mathcal{N}(-3.1, 0.1)$ and spatially vary along an $N_{\text{side}} = 16$ grid. We found that this was the highest resolution resolution grid in which the spectral index was not prior dominated across all high-latitude regions. In Fig. 11, we display the mean of all of the Gibbs samples, along with the standard deviation evaluated per each CG1 Gibbs sample, $\sigma_{\beta_s}^{\text{stat}}$, and the standard deviation over all CG1 samples and Commander1 samples, $\sigma_{\beta_s}^{\text{sys+stat}}$. Put concretely, $\sigma_{\beta_s}^{\text{stat}}$ is the standard deviation when the input maps themselves are static, and $\sigma_{\beta_s}^{\text{sys+stat}}$ includes variations in the frequency maps themselves, corresponding to underlying instrumental effects, including gain, noise characterization, and baseline estimation. The uncertainty due to white noise alone traces the high signal-to-noise regions of the polarized synchrotron, especially the prominent loops and spurs and the Fan region. At high Galactic latitudes, the standard deviation is 0.1, indicating that the posterior uncertainty is limited by the prior. To test this more concretely, we performed additional Commander1 runs with priors of $\mathcal{N}(-3.2, 0.1)$ and $\mathcal{N}(-3.0, 0.1)$, and used the deviation from the mean in the fiducial analysis as an estimate of the extent of prior domination, $\sigma_{\beta_s}^{\text{prior}} \equiv (\langle \beta_{-3.0} \rangle - \langle \beta_{-3.2} \rangle)/2$. Adding this in quadrature, this gives the total uncertainty, which we display in the bottom panel of Fig. 11.

The uncertainty across the entire Gibbs chain does not merely trace high signal-to-noise regions, and in fact there are variations that exceed the prior surrounding the Galactic center. These variations are primarily due to gain and bandpass uncertainties. It therefore makes sense that gain variations in *K*, *Ka*, and 30 GHz around the brightest region of the sky would induce a large variations. Despite the relative increase in noise level when including instrumental effects, the brightest Galactic loops, the Cygnus region, and Tau A regions are well-constrained by the data.

As a final quality check, we display the residuals with respect to the Commander1 sky model in Fig. 12, as well as the total scaled and normalized χ^2 . In all bands but *K*, 30 GHz, and *Ka*, there are no visible artifacts due to instrumental uncertainty, with each map showing fluctuations consistent with the estimated white noise level calculated in the DR1 processing. In addition, many of the residuals visible in Fig. 3 have been reduced, demonstrating that polarized synchrotron spectral index

⁷ <https://github.com/Cosmoglobe/Commander1>

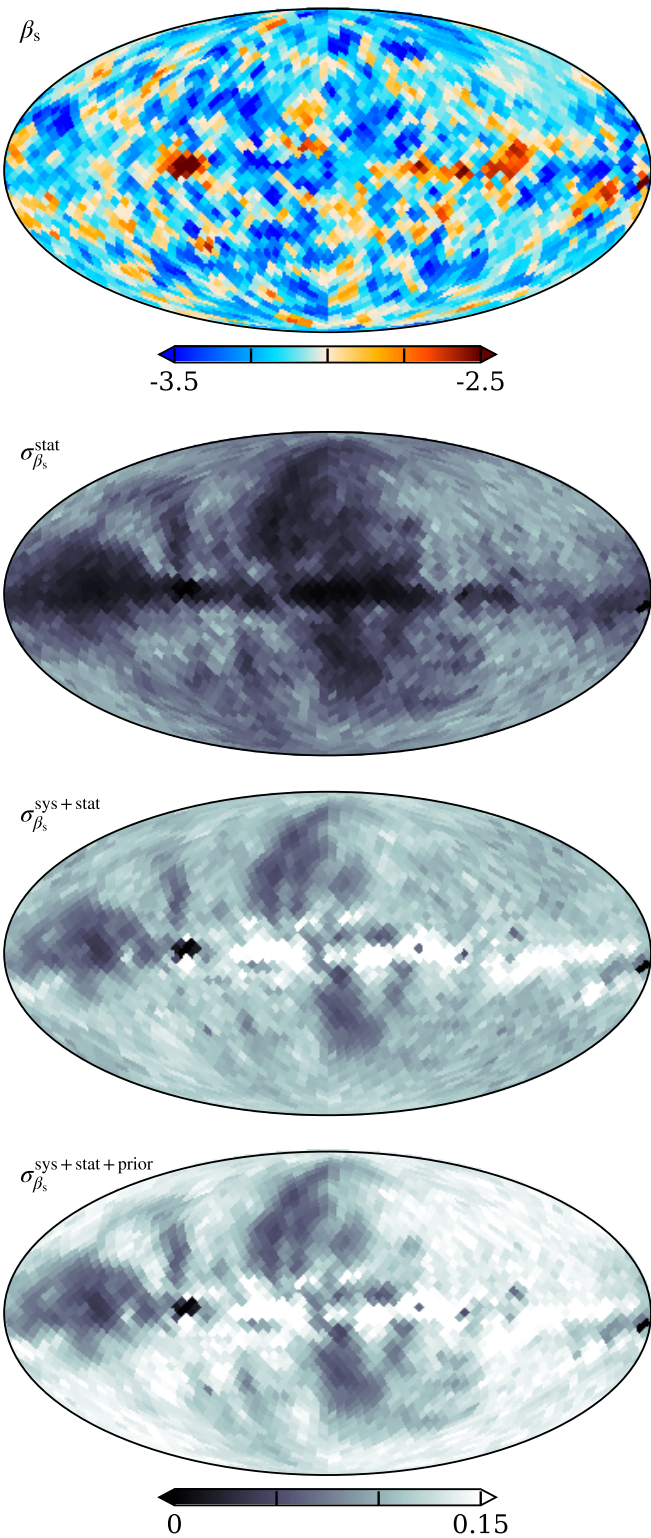


Fig. 11. Commander1 β_s constraints. (First): Mean spectral index over all samples, (second): standard deviation over a single CG DR1 sample, (third): standard deviation over all Commander1 and CG DR1 samples, and (fourth): difference due to prior choice added in quadrature.

variation provides meaningful improvements to the sky model fit.

The most salient remaining residuals are in K , 30 GHz, and Ka . K -band and 30 GHz are anticorrelated surrounding Galactic center, indicating tension between these two high signal-to-noise datasets. This could either be due to genuine mismodeling of the sky, or be due to incompletely modelled instrumental parameters. In particular, the signature is reminiscent of bandpass leakage corrections, which are shown, e.g., in Fig. 9 of Svalheim et al. (2023b).

A more persistent residual is found in the Stokes Q Ka -band map. This feature has appeared in several different analyses, e.g., Fig. 4 of Svalheim et al. (2023a) and Fig. 8 of Weiland et al. (2022), but was not as clear without full removal the poorly measured modes in the final map. The lack of this feature in the corresponding Stokes U map suggests that the effect is not a true Galactic effect, and is in some way due to instrumental processing, or unmodeled systematics. We discuss potential sources of this signal in Sec. 5.

5. Discussion and conclusion

We have presented the state-of-the-art model of polarized synchrotron model using the COSMOGLOBE DR1 data products. The polarized synchrotron map as delivered in Watts et al. (2023a) has an effective white noise level of $3.4 \mu\text{K}$, a 29 % improvement over the white noise levels of the *WMAP* K -band and LFI 30 GHz maps. Using the fully consistent reprocessed *WMAP* and *Planck* LFI data, we have been able to leverage the full statistical power of both datasets. We have additionally verified that this model characterizes the polarized sky signal to within $5 \mu\text{K}$ at all bands. We have also reproduced the previously-reported E -to- B -mode ratio in the polarized synchrotron ratio. Furthermore, we have shown that physically reasonable spectral indices can be recovered using a variety of methods, which are consistent with both the methods presented in this paper and with previously published results from CLASS and QUIJOTE, confirming variation in β_s along the Galactic plane and constant at high Galactic latitudes.

Our improved processing of the *WMAP* and LFI data in conjunction with improved polarized synchrotron modeling has allowed us to dig deeper into the underlying differences between the two datasets. We have shown agreement between the β_s values derived using the T-T plot method that are in agreement within the expected uncertainties using $K/30$ GHz and K/Ka data combinations, further evidence that these datasets are now consistent with each other. The remaining unexplained differences between the sky maps and our derived model are primarily in the Galactic center, and have morphologies consistent with bandpass errors and SED complexities.

The least well-understood residual is in the Ka -band, specifically Stokes Q . Of all the known instrumental effects in both *WMAP* and *Planck* LFI, the only one that morphologically resembles this residual is the bandpass correction in K -band, which was previously presented in Figure 12 of Watts et al. (2023a). The bandpass correction term depends on accurate laboratory measurements, presented in Jarosik et al. (2003). The high statistical weight of K -band for determining polarized synchrotron could easily lead to an undersubtraction in the Ka -band maps. Conversely, the bandpass correction to Ka -band itself is negligible, as all of the Ka -band radiometers were reported to have nearly identical bandpasses. A full accounting of this effect, including sampling of bandpass differences in the *WMAP*

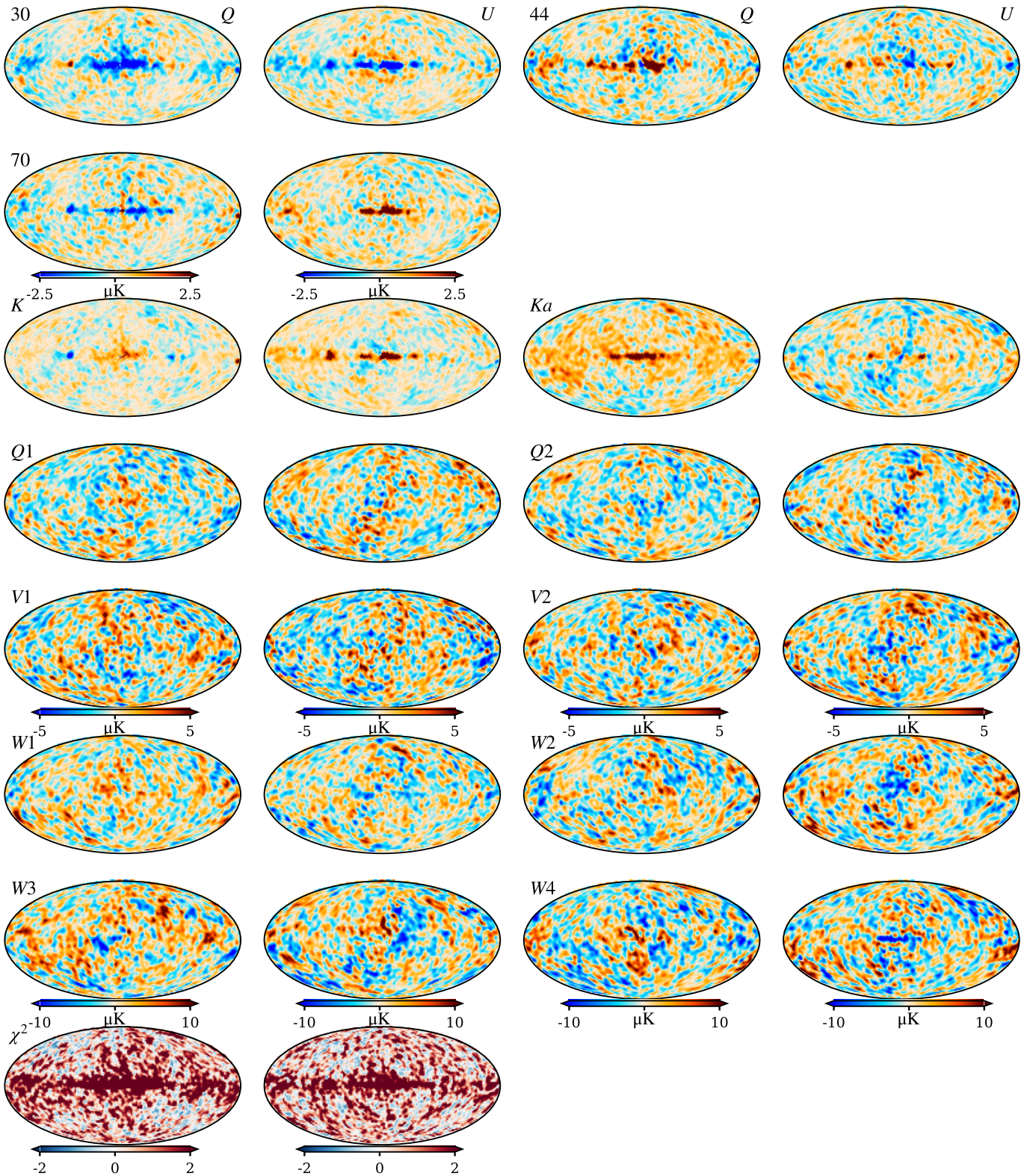


Fig. 12. Residual maps and normalized χ^2 . Panels are organized with LFI channels in rows 1–2, WMAP in rows 3–7, and the total reduced χ^2 in row 8.

TOD's (not performed in Watts et al. 2023a) will be performed in future work.

The estimation of β_s is difficult precisely because the quantity is dependent on differences between different frequencies, which can often exacerbate systematic effects and processing

choices. The differences between a sky model and datasets is best determined in the timestreams – much of the improvement demonstrated in this analysis would not have been possible through a purely map-based analysis. Beyond pure improvement of data quality, this approach allowed for a natural end-to-end

propagation of errors, and demonstrated that some of the brightest regions of the sky in fact do not have well-determined spectral indices, despite their high signal-to-instrumental noise ratio. As increasingly stringent uncertainty constraints are becoming necessary in order to measure a non-zero tensor-to-scalar ratio, the use of joint information between experiments with complementary observation strategies will increasingly become a necessity. Future joint analysis, including for example QUIJOTE and CLASS data, will continue to improve our knowledge of the polarized sky.

References

- Alonso, D., Sanchez, J., Slosar, A., & LSST Dark Energy Science Collaboration. 2019, MNRAS, 484, 4127
 Basyrov, A., Suur-Uski, A.-S., Colombo, L. P. L., et al. 2023, A&A, 675, A10
 Bennett, C. L., Banday, A. J., Gorski, K. M., et al. 1996, ApJ, 464, L1
 Bennett, C. L., Larson, D., Weiland, J. L., et al. 2013, ApJS, 208, 20
 BeyondPlanck Collaboration. 2023, A&A, 675, A1
 BICEP2/Keck Array and Planck Collaborations. 2015, Phys. Rev. Lett., 114, 101301
 de Belsunce, R., Gratton, S., & Efstathiou, G. 2022, MNRAS, 517, 2855
 de la Hoz, E., Barreiro, R. B., Vielva, P., et al. 2023, MNRAS, 519, 3504
 de la Hoz, E., Diego-Palazuelos, P., Martínez-González, E., et al. 2022, J. Cosmology Astropart. Phys., 2022, 032
 Delabrouille, J., Betoule, M., Melin, J.-B., et al. 2013, A&A, 553, A96
 Eimer, J. R., Li, Y., Brewer, M. K., et al. 2023, arXiv e-prints, arXiv:2309.00675
 Fuskeland, U., Andersen, K. J., Aurlien, R., et al. 2021, A&A, 646, A69
 Fuskeland, U., Wehus, I. K., Eriksen, H. K., & Næss, S. K. 2014, ApJ, 790, 104
 Galloway, M., Andersen, K. J., Aurlien, R., et al. 2023, A&A, 675, A3
 Haslam, C. G. T., Salter, C. J., Stoffel, H., & Wilson, W. E. 1982, A&AS, 47, 1
 Jarosik, N., Barnes, C., Greason, M. R., et al. 2007, ApJS, 170, 263
 Jarosik, N., Bennett, C. L., Halpern, M., et al. 2003, ApJS, 145, 413
 Krachmalnicoff, N., Carretti, E., Baccigalupi, C., et al. 2018, A&A, 618, A166
 Neronov, A., Malyshev, D., & Semikoz, D. V. 2017, A&A, 606, A22
 Orear, J. 1982, American Journal of Physics, 50, 912
 Orlando, E. & Strong, A. 2013, MNRAS, 436, 2127
 Page, L., Hinshaw, G., Komatsu, E., et al. 2007, ApJS, 170, 335
 Planck Collaboration X. 2016, A&A, 594, A10
 Planck Collaboration I. 2020, A&A, 641, A1
 Planck Collaboration II. 2020, A&A, 641, A2
 Planck Collaboration IV. 2018, A&A, 641, A4
 Planck Collaboration V. 2020, A&A, 641, A5
 Planck Collaboration Int. LVII. 2020, A&A, 643, A42
 Rubiño-Martín, J. A., Guidi, F., Génova-Santos, R. T., et al. 2023, MNRAS, 519, 3383
 Rybicki, G. B. & Lightman, A. P. 1985, Radiative Processes in Astrophysics (New York, NY: Wiley)
 Svalheim, T. L., Andersen, K. J., Aurlien, R., et al. 2023a, A&A, 675, A14
 Svalheim, T. L., Zonca, A., Andersen, K. J., et al. 2023b, A&A, 675, A9
 Thorne, B., Dunkley, J., Alonso, D., & Næss, S. 2017, MNRAS, 469, 2821
 Watts, D. J., Basyrov, A., Eskilt, J. R., et al. 2023a, arXiv e-prints, arXiv:2303.08095
 Watts, D. J., Galloway, M., Ihle, H. T., et al. 2023b, A&A, 675, A16
 Wehus, I. K., Fuskeland, U., & Eriksen, H. K. 2013, ApJ, 763, 138
 Weiland, J. L., Addison, G. E., Bennett, C. L., Halpern, M., & Hinshaw, G. 2022, ApJ, 936, 24
 Weiland, J. L., Osumi, K., Addison, G. E., et al. 2018, ApJ, 863, 161
 Zonca, A., Thorne, B., Krachmalnicoff, N., & Borrill, J. 2021, Journal of Open Source Software, 6, 3783

Appendix A: T-T Plots

This section shows two intermediate results in the T-T plot analysis. Figure A.1 shows the scatter plots within each individual region for both the *WMAP9* and COSMOGLOBE DR1 results, while Fig. A.2 shows the measured spectral index as a function of polarization angle α . For more details, the interested reader can consult [Fuskeland et al. \(2014\)](#).



Fig. A.1. T-T plots for Stokes Q and U maps of the COSMOGLOBE 23 GHz versus the COSMOGLOBE 30 GHz (black) and the 9 yr *WMAP* 23 GHz versus *Planck* 2018 30 GHz (red) for all regions. The horizontal (solid and dotted) lines indicates the corresponding inverse variance weighted values of the spectral index, averaged over rotation angle, and in the COSMOGLOBE case also samples.



Fig. A.2. Synchrotron spectral index as a function of rotation angle, computed using T-T plot between the COSMOGLOBE 23 GHz and the COSMOGLOBE 30 GHz (black) compared to the spectral index using the 9 yr WMAP 23 GHz and *Planck* 2018 30 GHz (red) for all regions. The horizontal (solid and dotted) lines indicates the corresponding inverse variance weighted values of the spectral index, averaged over rotation angle, and in the COSMOGLOBE case also samples.